PNAS RESEARCH ARTICLE | MEDICAL SCIENCES

Small-molecule disruption of androgen receptor–dependent chromatin clusters

Sarah E. Kohrt[a,b], Emily J. Novak[b], Subhashish Tapadar[c], Bocheng Wu[c], Jonathan Strope[d], Yaw Asante[a,e], Hyunmin Kim[a], Matthew S. Chang[f], Douglas Gurdak[f], Athar Khalil[f], Michael Rood[g], Eric Raftery[c], Diana Stavreva[h], Holly M. Nguyen[i], Lisha G. Brown[i], Maddy Ramser[d], Cody Peer[d], Warren M. Meyers[j], Nicholas Aboreden[k], Maharshi Chakravortee[l], Richard Sallari[l], Peter S. Nelson[m,n,o], Kathleen K. Kelly[p], Thomas G. W. Graham[q], Xavier Darzacq[q], William D. Figg[d], Adegboyega K. Oyelere[c,1], Eva Corey[j,1], Remi Adelaiye-Ogala[r,1], and Berkley E. Gryder[a,f,1]

Affiliations are included on p. 10.

Edited by Myles Brown, Dana-Farber Cancer Institute, Boston, MA; received March 26, 2024; accepted October 22, 2024

Sustained androgen receptor (AR) signaling during relapse is a central driver of metastatic castration-resistant prostate cancer (mCRPC). Current AR antagonists, such as enzalutamide, fail to provide long-term benefit for the mCRPC patients who have dramatic increases in AR expression. Here, we report AR antagonists with efficacy in AR-overexpressing models. These molecules bind to the ligand-binding domain of the AR, promote AR localization to the nucleus, yet potently and selectively down-regulate AR-target genes. The molecules BG-15a and the pharmacokinetically optimized BG-15n elicit a decrease in cell and tumor growth in vitro and in vivo in models of mCRPC. BG-15a/n treatment causes the collapse of chromatin loops between enhancers and promoters at key genes in the AR-driven epigenome. AR binding in the promoter, as well as 3D chromatin clustering, is needed for genes to respond. BG-15a/n represent promising agents for treating patients with relapsed AR-driven mCRPC tumors.

chromatin architecture | androgen receptor | prostate cancer | epigenetics | gene regulation

Significance

Prostate cancer patients who undergo androgen-deprivation therapy (ADT) and treatment with androgen receptor (AR) antagonists, such as enzalutamide, will inevitably progress to aggressive metastatic castration-resistant prostate cancer (mCRPC). This study presents AR antagonists that promote AR translocation to the nucleus and initiate AR binding to chromatin, but effectively block AR-driven transcription. These compounds demonstrate superior anticancer activity across a spectrum of AR-driven cell lines and LuCaP patient-derived xenograft models of mCRPC in vitro and are effective in vivo. AQuA-HiChIP reveals a collapse of 3D chromatin clusters upon treatment with these AR antagonists, providing unique insights into the epigenetic vulnerabilities of mCRPC.

Prostate cancer remains the most common cancer among males in the United States, with African American men at the highest risk (1). It is also the second leading cause of cancer-related death for men in the United States, largely due to the progressively treatment-resistant nature of the disease. Metastatic castration-resistant prostate cancer (mCRPC), the final stage of the disease, continues to elude treatment and claims the lives of more than thirty thousand men every year in the United States. Primary prostate cancer and the majority of mCRPC tumors depend on the androgen receptor (AR) signaling pathway. In this pathway, androgen ligands, like testosterone, bind to the AR to activate aberrant transcriptional programs in prostate cancer cells. Treatment options for prostate cancer commonly involve various combinations of radical prostatectomy, radiation therapy, and critically, androgen-deprivation therapy (ADT) (2). However, the disease frequently advances to the lethal mCRPC, caused among other mechanisms by either AR mutation, emergence of constitutively active AR splice variants (3), transdifferentiation to neuroendocrine prostate cancer (4), or, most often, by overexpressing AR (5, 6). The expression levels of AR are at least six-fold higher in mCRPC when compared to primary prostate cancer (7). This is most commonly achieved by the amplification of the AR and/or its enhancers (8).

Nuclear receptors, such as the AR, are ligand-dependent transcription factors (TFs) that confer cell identity, guide developmental differentiation, and maintain homeostasis in adult tissues (9). These receptors are central drivers in diverse cancer types (10). In AR-responsive tissues, steroid agonists, such as testosterone, bind to the ligand-binding domain of AR causing the AR-ligand complex to dimerize and translocate to the nucleus. Agonist-bound AR dimers bind to chromatin at promoters and enhancers (11, 12) and recruit diverse chromatin regulatory and binding partners [BAF (13), p300 (14), and NCoA (15)] necessary to activate transcription (16).

First- and second-generation therapeutics for AR-driven mCRPC can reduce the levels of circulating androgens, such as abiraterone acetate, or block androgen binding to AR, such as bicalutamide or enzalutamide. Androgen-receptor signaling inhibitors (ARSI) as agents for prostate cancer therapy are well tolerated; however, the ARSI in common clinical use lose their impact in Mcrpc (17–19). Compounds RD162 (20), apalutamide (ARN-509) (21), and darolutamide (22) are recent examples of ARSIs that exceed bicalutamide and enzalutamide in their ability to antagonize the AR signaling. However, these ARSIs still offer only a mild improvement in patient outcomes and do not evade treatment resistance (23, 24). The efficacy of current therapeutics is circumvented by tumor cells through a

Competing interest statement: E.C. received research funding under institutional SRA from Janssen Research and Development, Bayer Pharmaceuticals, KronosBio, Forma Pharmaceutics Foghorn, Gilead, Sanofi, AbbVie, MacrogGenics, Astra Zeneca, GSK, and K36. B.E.G., A.K.O., S.T., W.D.F., and J.S. are co-inventors on a patent covering this technology (WO2021150603A1). P.S.N. receives personal fees from Janssen, Bristol Myers Squibb, Pfizer, and Merck and grants from Janssen. The other authors declare no competing interests.

This article is a PNAS Direct Submission.

[1]To whom correspondence may be addressed. Email: adegboyega.oyelere@chemistry.gatech.edu, ecorey@uw.edu, remiadel@buffalo.edu, or berkley.gryder@case.edu.

This article contains supporting information online at https://www.pnas.org/lookup/suppl/doi:10.1073/pnas.2406239121/-/DCSupplemental.

Published November 19, 2024.

variety of mechanisms that converge on increasing the basal levels of AR activity, enabling tumor cells to become independent of androgen levels. The diminished efficacy of existing ARSIs is partly due to a switch to agonist activities on some AR mutants (25), but most commonly, their antagonist activities are weakened when AR is amplified (8). Importantly, even when ADT is circumvented, AR remains central in driving tumor progression in the majority of the mCRPC tumors, and prostate cancer cells remain highly dependent on the AR in genetic CRISPR screens (*SI Appendix*, Fig. S1*A*). The AR therefore remains a viable target for further therapeutic perturbation with a focus on overcoming resistance mechanisms.

In this work, we have developed AR antagonists that actively induce AR nuclear localization, induce AR binding to chromatin, collapse AR-dependent chromatin clusters, shut down transcription of AR target genes, and have improved efficacy over current ARSIs in mCRPC models.

Results

Optimization and Identification of AR-Targeting Molecules. Prior studies using ARSIs in dual-targeting constructs taught us that the three-nitrogen-containing heteroaromatic ring, triazole, is compatible with AR binding, enabling click-chemistry campaigns (26, 27). Thus, we explored pure aryl hydantoin triazoles with a cyanonilutamide scaffold in the base, resembling enzalutamide, but diversified the structure at the solvent-exposed exterior (Fig. 1*A* and *SI Appendix*, Table S1). The synthesized compounds were evaluated for the ability to inhibit AR-signaling using AR-binding and transcription-based assays (further details on chemical synthesis are found in *SI Appendix*, *Supplementary Discussion*). Iterative rounds of medicinal chemistry altering the cyanonilutamide scaffold base of enzalutamide identified four sites of distinct function in AR targeting molecules. When optimized, the resulting molecule, BG-15a, demonstrated improved efficacy and prompted an investigation into the mechanism of action.

First, the orientation of the triazole head group was required for anti-AR transcriptional activity. We hypothesized that the efficacy of compound BG-15a could be destabilized by disrupting the hydrogen binding of the triazole head group (Fig. 1 *A*, R2). Upon addition of a single methyl group, we observed a dramatic loss in activity (compound 15b, *SI Appendix*, Fig. S1*B*). This loss of activity was rescued by the reintroduction of hydrogen bond donor and acceptor atoms via a terminal alcohol in reverse triazoles 18b-e (*SI Appendix*, Fig. S1*C*). Additionally, whereas the simple hydrogen extension from a reverse triazole 18a exhibited no significant improvement over the azide 17, the introduction of a hydrogen bond capable amine in 19 resulted in a complete AR antagonism, more potent than bicalutamide, enzalutamide, and cyanonilutamide (*SI Appendix*, Fig. S1*C*). The efficacy of amine 19 was dampened by conversion to amide 20 (*SI Appendix*, Fig. S1*C*). Next, we directly compared the impact of oxygen-sulfur swapping and of hydrogen-methyl swapping, showing that the inclusion of sulfur in the hydantoin ring is superior, and retention of 1H in the triazole is essential, delineating the important molecular features of BG-15a (Fig. 1*B*).

The solubility of BG-15a was limited, and suboptimal pharmacokinetic properties were suspected. To address this issue, we performed chemical informatic analysis of atomic substitutions that improve the water solubility without altering the chemical features established in AR-transcriptional studies. We designed BG-15n with a nitrogen as an additional hydrogen bond acceptor in the base aromatic ring, while retaining the critical triazole and thiohydantoin features, thus improving 10-fold the calculated octanol:water partition coefficient and resulting in solubility in our aqueous formulation for in vivo studies (Fig. 1*C* and *SI Appendix*, Fig. S2 *A* and *B*). A similar strategy was employed in the development of ARSI apalutamide (28).

BG-15a and BG-15n both exhibit strong AR binding affinity (*SI Appendix*, Fig. S3*A*). Importantly, BG-15a/n retained high AR selectivity compared to other nuclear hormone receptor family members (*SI Appendix*, Fig. S3 *A–D*). The progesterone receptor (PR) is another member of the steroid hormone group of the nuclear receptor family and shares more than 80% sequence homology with AR (29). Given the high structural homology, it is not surprising that testosterone also binds to PR (although not dihydrotestosterone) (29). In our radioligand binding assays, BG-15a and BG-15n show nanomolar range binding affinity to the PR (*SI Appendix*, Fig. S3 *B–D*). However, the cell models used in this study do not express *PGR* (*SI Appendix*, Fig. S3*E*), precluding confounding results of polypharmacology.

Leveraging crystal structures of the AR-ligand-binding domain (LBD) (30), AR dimer structures (31), and AI-generated models of the AR alpha helix Tau1 (32), we constructed a homology model of a dimer of AR LBD bound to the AR Tau1 domain (Fig. 1*E*, in the presence of BG-15a). Using Vina (33), we docked BG-15a/n to the ligand-binding pocket exposed by moving helix 12, exhibiting higher in silico affinity to AR than DHT. In the pocket, BG-15a/n formed anchoring hydrogen bonds with R753, Q712, and E710 (Fig. 1*F*). Moreover, BG-15a/n outperformed enzalutamide in inhibiting AR-driven luciferase transcriptional activity in VCaP prostate cancer cells (Fig. 1*G*).

Small Molecules Cause a Loss of Transcriptional Activity Despite Nuclear Localization. Dose–response combination matrix of AR-driven luciferase showed that the largest response to BG-15a was at 10 nM of R1881 (Fig. 2 *A*, *Left*). Further investigation showed a dose-dependent decrease of AR activity upon treatment with BG-15a, BG-15n, or enzalutamide in media supplemented with AR agonist (Fig. 2 *A*, *Right*). The data indicated that BG-15a/n are able to reduce AR-transcriptional output at lower concentrations than enzalutamide.

The clinical approval of enzalutamide was fueled by the observation that it had a distinct mode of action and therefore the promise of applicability in bicalutamide-resistant tumors (a major subset of mCRPC at that time) (20, 34, 35). Enzalutamide impairs helix 12 (H12) flexibility which prevents AR translocation to the nucleus and subsequent DNA binding to block transcriptional activation. Here, we show that BG-15a and BG-15n down-regulate AR-directed transcription yet, surprisingly, actively recruit AR into the nucleus. The results of the dose–response curves of nuclear translocation in murine 3,108 cells expressing GFP-AR (36) indicated that rigid (phenyl-based) AR binder BG-16, as well as enzalutamide, failed to induce AR translocation to the nucleus, whereas the flexible (benzyl-based) AR binder BG-15a induced nuclear translocation at doses 100 nM to 10 μM (Fig. 2*B*). Using a GFP-AR construct, we investigated the effect of our compounds on the nuclear translocation of AR in human cell lines. In the absence of ligand, the AR resides in the cytoplasm (Fig. 2*C*), and treatment with BG-15a and BG-15n consistently stimulated AR nuclear translocation (Fig. 2*C* and *SI Appendix*, Fig. S4 *A* and *B* and S5*A*). In contrast, there was a variability in enzalutamide's impact on nuclear translocation across different experiments (Fig. 2 *B* and *C* and *SI Appendix*, Fig. S4*A*).

We noted that in LNCaP-AR cells, AR formed concentrated puncta (Fig. 2*D* and *SI Appendix*, Fig. S5*A*). The size and shape of puncta have implications on the functions of the proteins at these sites (37). Quantification of the AR puncta demonstrated that

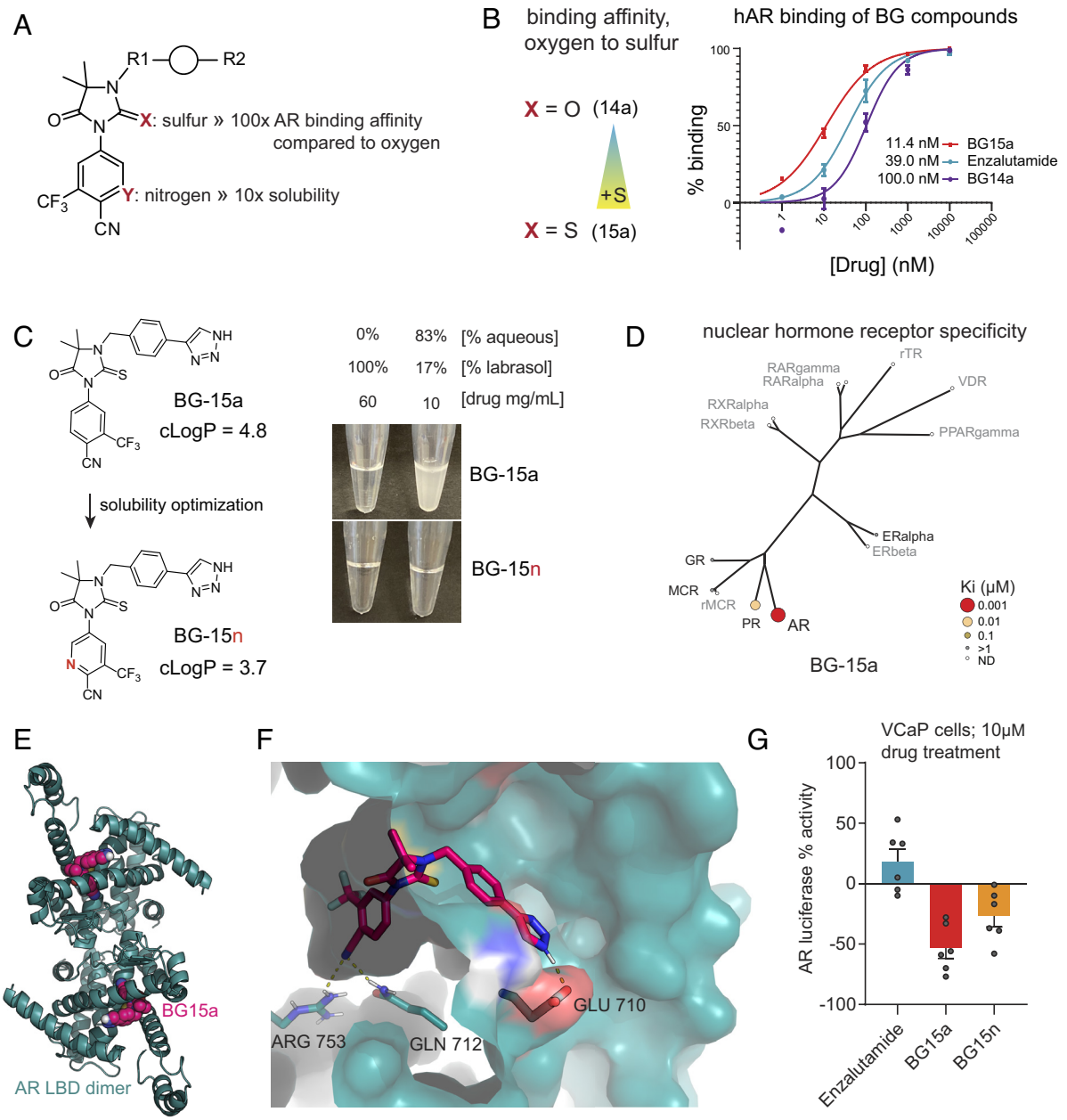

Fig. 1. Chemical determinants of AR-targeted activity. (*A*) Diagram showing the medicinal chemistry optimization strategy for the BG series of molecules described in this paper. (*B*) Small chemical modifications cause significant changes in AR binding affinity, such as the oxygen to sulfur change from 14a to 15a. (*C*) Chemical structure and calculated logP (octanol:water partition coefficient) of BG-15a and BG-15n. BG-15n has improved solubility compared to BG-15a and is therefore hypothesized to be more suitable for downstream in vivo studies. Compounds are dissolved in 100% labrasol or 1:6 dilution of labrasol in saline with 5% sucrose. (*D*) Phylogenic trees showing relationship of nuclear hormone receptors and affinity to BG-15a or BG-15n, compared to enzalutamide. Binding affinity measured by radioligand binding affinity assay in hAR with testosterone. Response average is a measure of nuclear receptor binding as Ki values in μM. (*E*) Proposed model of AR-ligand-binding domains interacting with an L/I-X-X-L/I-L/I motif, represented here by AR Tau1 helix, and forming a dimer in the presence of BG15a. (*F*) BG15a in the pocket of AR LBD and Tau1, with hydrogen bonds forming between the molecule and R753, Q712, and E710. (*G*) Modifications to improve solubility do not impede AR-transcriptional activity. The bar chart shows AR promoter-based luciferase assay [pAR-Luc (Signosis LR-2105)] in mCRPC cell line VCaP cells grown in CSS and 10 nM R1881 and dose with 10 μM of enzalutamide, BG-15a, or BG-15n.

BG-15n results in larger nucleic puncta compared to R1881 and control (Fig. 2*E* and *SI Appendix*, Fig. S5*B*). The quantification also confirmed that BG-15n results in AR-nuclear translocation similar to R1881 (Fig. 2*F*). We observed that the nuclear puncta in cells treated with R1881 and BG-15n were less circular compared to cytoplasmic puncta for R1881 and BG-15n treatment respectively, but there was no difference in nuclear R1881 versus nuclear BG-15n puncta circularity (*SI Appendix*, Fig. S5*D*). These results suggest the mechanism of BG-15n action may involve dysregulation of AR aggregation. Variability between each treatment nuclei was minimal (*SI Appendix*, Fig. S5 *E–G*). Importantly, despite the similarities between R1881- and BG-15n-driven AR-nuclear translocation, BG-15n treatment resulted in the downregulation of AR-target genes expression, including *KLK3* and *TMPRSS2* (Fig. 2*G*).

Therapeutic Efficacy In Vitro Is Driven by AR and MYC Gene Pathway Downregulation. Direct inhibition of AR-transcriptional activity should translate into therapeutic benefit. In LNCaP-AR and 22Rv1 cells, BG-15a and BG-15n were more efficacious in inhibiting growth compared to enzalutamide (Fig. 3*A* and *SI Appendix*, Fig. S6 *A* and *B*). Importantly, BG-15a/n exhibited

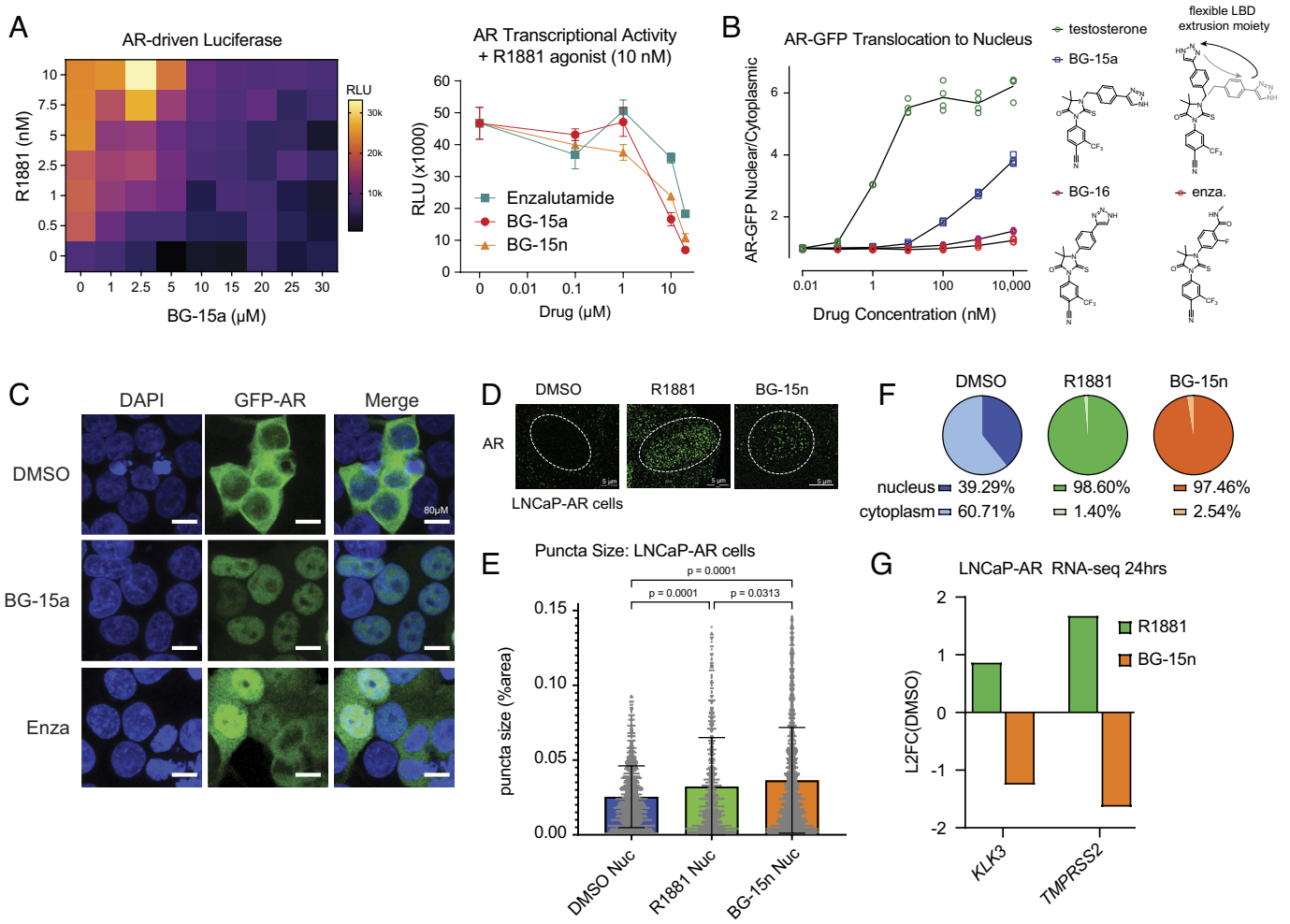

Fig. 2. Lead compounds decrease AR transcriptional activity while promoting localization into the nucleus. (*A*) *Left*: Heatmap of AR transcriptional activity measured by luciferase in a combination matrix dose response to R1881 and BG15-a in LNCaP cells grown in CSS. *Right*: Transcriptional activity of BG-15a, BG-15n, and enzalutamide in prostate cancer cell line VCaP, measured by AR-promoter-based luciferase assay in media supplemented with CSS and 10 nM of R1881. The line plot shows total detected luminescent signal normalized to vehicle signal. (*B*) AR-GFP cellular localization measured as nuclear to cytoplasmic ratio influenced by testosterone, enzalutamide, BG-15a, or BG-16 in murine cells (*Left*). Compound structures for enzalutamide, BG-15a, or BG-16 (*Right*), highlighting the flexible LBD extrusion moiety of BG-15a. (*C*) Exogenous GFP-AR construct in HEK293T cells treated with vehicle, BG-15a, or enzalutamide. Cells were grown in CSS. Nuclei are stained with DAPI. (*D*) Immunofluorescence staining of AR in LNCaP-AR cells (*Above*) at increased magnification and deconvolution showing AR puncta in the nucleus. Cells were stained with DAPI and with anti-AR antibodies. Nuclei are artificially circled with dotted white line. (*E*) Puncta size was calculated as a %area of each puncta over a threshold signal intensity compared to the entire image. Bar plots represent a sum of all nuclei per image with each point representative of a single puncta. $*P < 0.05$, $***P < 0.0001$. (*F*) Quantification of localization of AR puncta in the cytoplasm of the nucleus of each treatment group. Calculations are based on the signal intensity above a given threshold within or outside of the drawn nuclei as determined by the DAPI staining. (*G*) RNA-sequencing data from LNCaP-AR cells treated with R1881 or BG-15n. The expression level of AR target genes *KLK3* and *TMPRSS2* is shown as a log2 fold change compared to vehicle control.

inhibitory activity even in cells with AR mutations that confer enzalutamide resistance including 22Rv1 (*SI Appendix*, Fig. S6 *C* and *D*) and CWR-R1 EnzaRes (Fig. 3*B* and *SI Appendix*, Fig. S6 *E–I*) (38). To assess the efficacy of our lead molecules in a broader patient context, we performed growth inhibition assays evaluating the effects of BG-15a/n treatment on eight PCa and CRPC cell lines with diverse AR expression in dose response, measuring every 4 h over a week of cell growth (Fig. 3*C* and *SI Appendix*, Fig. S6 *J* and *K*). The results of these experiments further supported our conclusions that BG-15n exceeds enzalutamide inhibitory activity in multiple prostate cancer cell lines.

Given the inhibition of CRPC growth with BG-15a/n treatment, we hypothesized that BG-15a/n play an important role in disrupting the innate AR-transcriptional activity. To test the BG-15a/n effect on AR activity in models of diverse AR mutational and expression status, we performed RNA-seq analysis in a panel of PCa cell lines and LuCaP PDX models of mCRPC, choosing the dosing regimen with the most robust cell growth responses before complete cell loss (Fig. 3*D*). AR-dominant PCa was represented by 22Rv1 cells (CRPC cells with AR-V7 expression), LuCaP 70 (an ex vivo xenograft model), LNCaP-AR cells [LNCaP cells stably overexpressing AR-WT (39)], LAMP cells (LNCaP with resistance to enzalutamide by CRISPR-knock in of AR enhancer amplification), and LNCaP cells. The differential levels of AR expression among these models were predictive of the efficacy of BG-15n in reducing AR transcription (Fig. 3*D* and *SI Appendix*, Fig. S7*A*). PDX LuCaP 173.1 and cell line PC3 represented AR-negative PCa; in these models, BG-15n treatment was ineffective in decreasing the expression of androgen-responsive genes (Fig. 3*D*, gray highlight). Additionally, BG-15a and BG-15n were effective in decreasing multiple Hallmark gene sets including the mitotic spindle, MYC targets, G2M checkpoint, and E2F target genes across all of our AR+ models (Fig. 3*F* and *SI Appendix*, Fig. S7*A*).

The comparable RNA-seq profiles between BG-15a- and BG-15n-treated models indicated that the nitrogen substitution in the base aromatic ring did not alter the inhibitory effects on

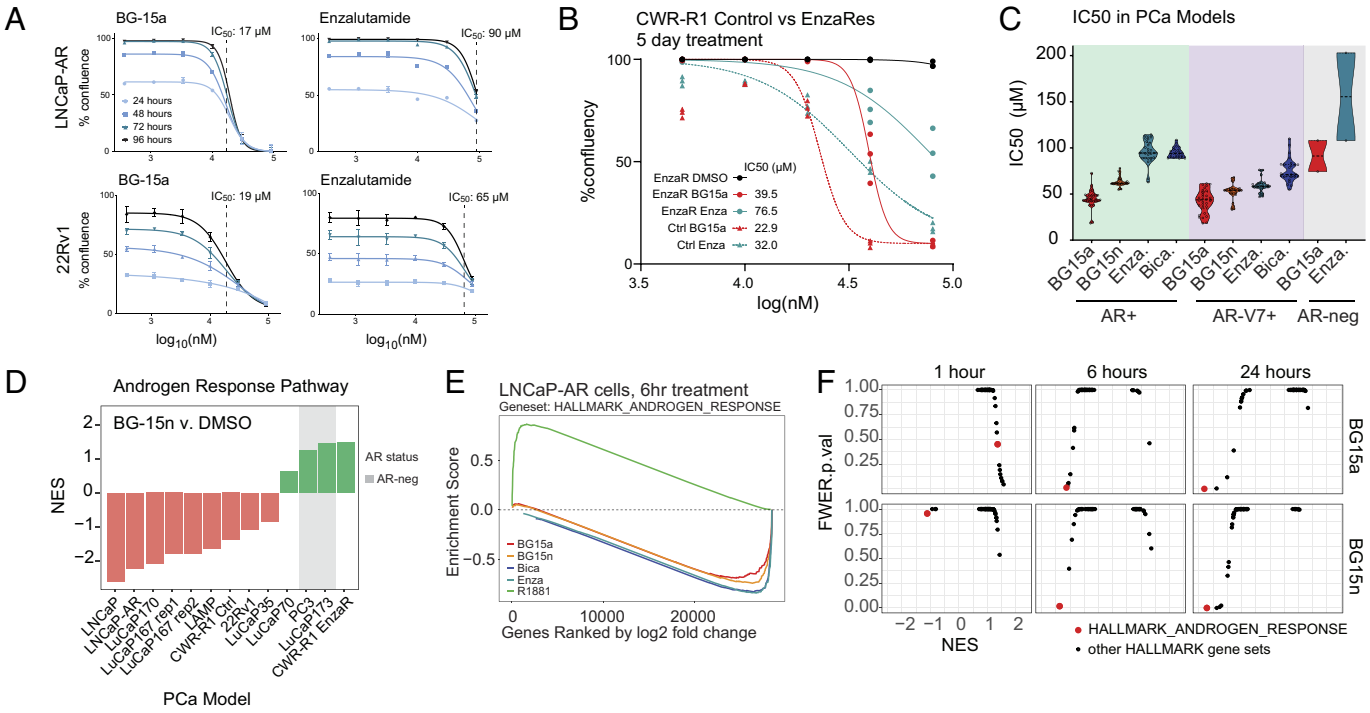

Fig. 3. AR antagonists reduce PCa cell growth and inhibit AR target genes. (*A*) Dose response of cell growth in LNCaP-AR cells (*Top*) and 22Rv1 cells (*Bottom*) treated with BG-15a (*Left*) or enzalutamide (*Right*). Cells were grown in regular FBS with no added androgens. Growth was measured as the percent cell confluence at 24, 48, 72, and 96 h. Error bars show the SE of measurement from triplicate wells. IC50 values are shown for the 72-h time point. (*B*) IC50 values for CWR-R1 cells that are controls or enzalutamide resistant treated with BG-15a or enzalutamide. BG-15a continues to be effective in enzalutamide-resistant cells. Cells were grown in regular FBS with no added androgens. (*C*) Violin plots of cumulative IC50 scores across AR-positive, AR-V7 positive, or AR-negative PCa cell lines. Point within plots represent different cell lines treated with BG15a, BG15n, enzalutamide, or bicalutamide. Median (solid black line) and quartiles (dotted black lines) are represented in each violin plot. Cells were grown in regular FBS with no added androgens. (*D*) RNA-sequencing data for a panel of PCa models treated with BG-15n represented as GSEA normalized enrichment scores (NES) for the Hallmark Androgen Response pathway. PCa models that are AR-negative are highlighted in gray. (*E*) GSEA analysis of the Hallmark Androgen Response geneset for LNCaP-AR cells treated for 6 h with R1881, BG-15a, BG-15n, enzalutamide, or bicalutamide. (*F*) Scatter plots of FWER p-values plotted against NES of GSEA analysis of the Hallmark Androgen Response geneset in a panel of CRPC cell lines and PDX models treated with BG-15a or BG-15n, compared to matched vehicle.

AR-transcriptional activity (Fig. 3*E*). Furthermore, as expected, comparison of BG-15n, BG-15a, enzalutamide, and bicalutamide, RNA-seq profiles demonstrates the inhibitory effects of all molecules on the Hallmark Androgen Response Pathway across a number of PCa models (*SI Appendix*, Fig. S7*B*). To quantify the dose dependence of the transcriptome alterations, we treated LNCaP-AR cells with increasing amounts of BG-15n (10 μM, 20 μM, 30 μM) for 24 and 48 h. The analysis revealed that even at the lowest dose and earliest time point, BG-15n had a robust and specific inhibitory effect on the Androgen Response pathway genes first, compared to other gene set pathways (*SI Appendix*, Fig. S8*A*). A shorter time course (1, 6, and 24 h) further demonstrates a robust inhibition of the expression of Androgen response genes by BG-15a and BG-15n in LNCaP-AR cells, and these responses were comparable to enzalutamide and bicalutamide response (Fig. 3*E* and *SI Appendix*, Fig. S8*B*). The androgen response, G2M, E2F, and MYC gene sets were all minimally altered at 1 h, then all were down-regulated at 6 and 24 h by BG-15a/n, whereas enzalutamide and bicalutamide while similarly impacting the AR pathway did not alter the expression of genes in MYC/G2M/E2F pathways (Fig. 3*F* and *SI Appendix*, Figs. S8*C* and S9).

Optimized Molecule BG-15n Is Orally Bioavailable and Effective In Vivo. In our first in vivo experiments, BG-15a showed inhibition of tumor growth in the AR-driven xenograft of LAPC4 (*SI Appendix*, Fig. S11*A*). However, it was difficult to fully dissolve BG-15a in the vehicle. We therefore turned to using only BG-15n that has better aqueous solubility for in vivo experiments. In a series of AR-positive PDX models, cultured ex vivo for 5 d, BG-15n exhibited increased efficacy compared to enzalutamide (Fig. 4 *A* and *B* and *SI Appendix*, Fig. S10). To capture the response of AR-positive mCRPC in vivo, we used the LuCaP 167 PDX model and showed that BG-15n effectively inhibited tumor progression (Fig. 4*C*). We then performed RNA-seq analysis of control- and BG-15n-treated tumors to interrogate the transcriptional effect in vivo. BG-15n decreased expression of Hallmark Androgen Response genes compared to vehicle (Fig. 4*D*). BG-15n treatment was safe for in vivo models as mouse body weight was not significantly decreased (*SI Appendix*, Fig. S11*B*) and no physical signs of distress were observed.

We next evaluated the pharmacokinetics/dynamics of BG-15a and BG-15n to determine the best compound for preclinical testing and further clinical development. We compared BG-15a and BG-15n head-to-head for abundance in circulating blood over time a course after oral gavage (Fig. 4*E*) or intravenous injection (Fig. 4*F*), finding this single atom substitution improved the pharmacokinetic profile, with greater circulating concentrations. Enzalutamide has a notably high half-life in patients at around 5 days once peak concentration is reached (40). This high half-life was noted in our in vitro studies, and BG-15a and BG-15n also show a notably high half-life in comparison to control compounds (Fig. 4*G*). BG-15n and BG-15a performed similarly to each other and enzalutamide in drug recovery and cell permeability assays (Fig. 4*H*) as well as clearance, absorption rate (*SI Appendix*, Fig. S11 *C* and *D*). To measure off-target cardiac effects, BG-15n and BG-15a were compared to enzalutamide and positive controls for binding to ion channels. All tested molecules were ineffective binders to hCaV1.2 and hNaV1.2 but did bind to hERG at high concentrations (Fig. 4*I*).

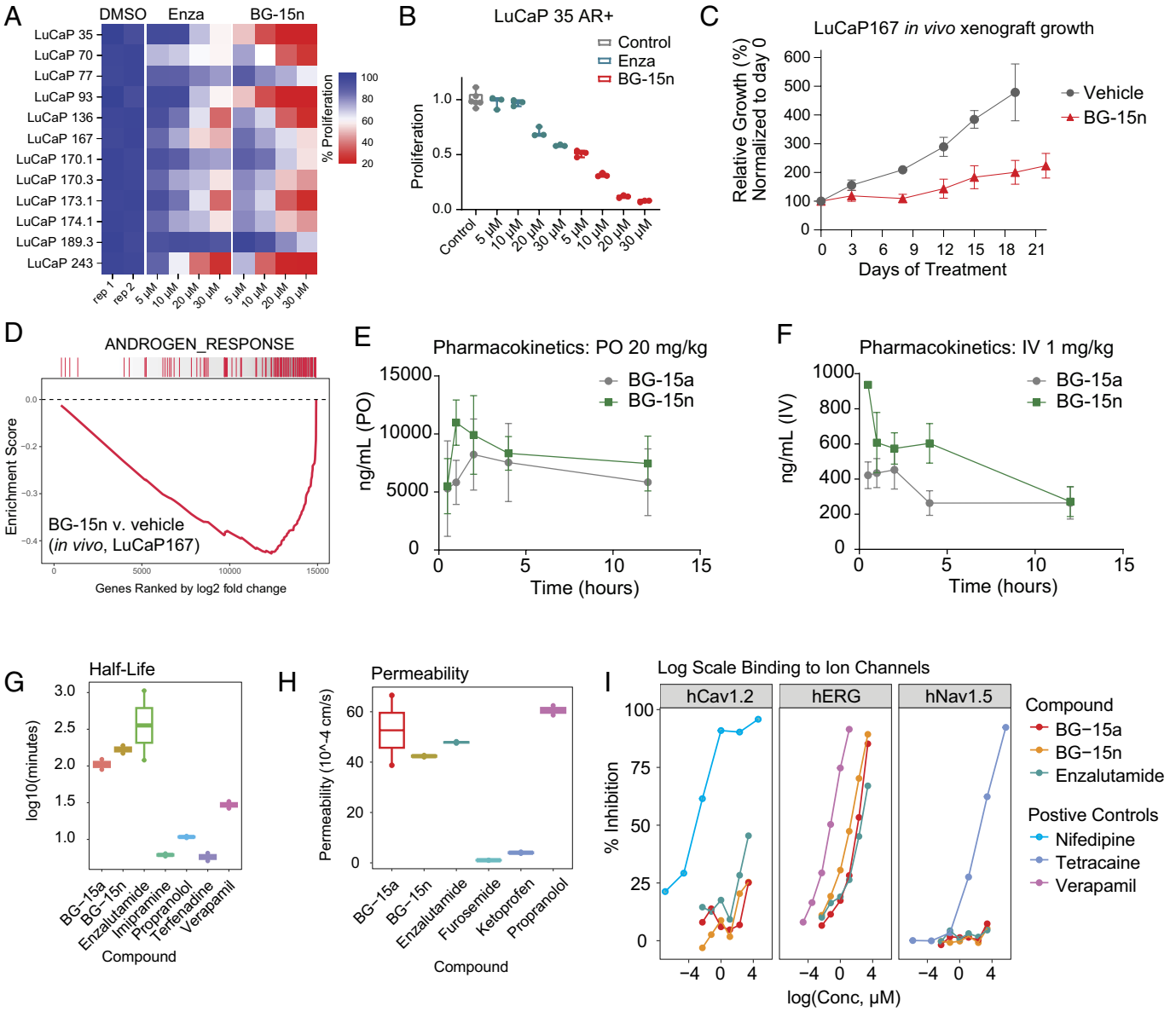

Fig. 4. Preclinical efficacy, bioavailability, and safety. (*A*) Heatmap of proliferation in LuCaP models in dose response of enzalutamide and BG-15n ex vivo after 5 d of treatment. (*B*) Boxplot of LuCaP 35 PDX ex vivo proliferation change by day 5 of control compared to increasing concentrations of enzalutamide or BG-15n treatment. In box plots, the center line shows median, box edges mark quartiles 1 and 3, and whiskers span minimum to maximum range. (*C*) Plot of LuCaP167 PDX grown in vivo over the course of 3 wk of treatment with vehicle or BG-15n at 20 mg/kg. Xenograft growth is displayed as a relative growth percentage normalized to treatment day 0 size. (*D*) GSEA hallmark response of the Hallmark Androgen Response Pathway geneset from in vivo LuCaP167 tumors. The curve represents log2(fold change) for BG-15n compared to DMSO. (*E* and *F*) Pharmacokinetics of BG-15a and BG-15n after 20 mg/kg oral gavage (PO, *E*) and 1 mg/kg intravenous injection (IV, *F*) over 12 h. Error bars represent the SD in ng/mL from three independent mice per time point. (*G*) Microsome metabolic assay results represented as the calculated half-life of the molecules. (*H*) Results of a Parallel Artificial Membrane Permeability Assay (PAMPA, pH 6.5) to show permeability (*Left*) of the molecules into a cell and the percentage of molecule recovered (*Right*). (*I*) Binding of test compounds BG-15a and BG-15n compared to enzalutamide and positive controls in ion channel assays, represented as % inhibition.

Collapse at AR-Dependent 3D Clusters of Active Chromatin. BG-15a/n induced AR-nuclear localization and yet inhibited AR-dependent transcription. We therefore hypothesized that the AR ability to bind to the DNA was being modulated at the chromatin level. We utilized a proximity-assisted photoactivation (PAPA) and fast single-molecule tracking assay (fSMT, Fig. 5 *A*, *Left*) (41) to evaluate AR self-association on chromatin. BG-15n increased both, AR self-association and AR-chromatin binding in live cells, in contrast to enzalutamide that did not (Fig. 5 *A*, *Right*). To track AR binding to DNA we performed ChIP-qPCR of the AR at the PSA enhancer region and AR HiChIP in LNCaP-AR cells at 1, 6, and 24 h of BG-15n treatment. BG-15n promoted an increase in AR binding signal after 1 h of treatment, then decreased over time (Fig. 5*B*). This led us to hypothesize that a decrease in acetylation, and thus loss of chromatin activity, is involved in the decrease in transcription of AR-target genes by BG-15n. Analysis of CUT&RUN (42) for H3K27ac, a mark of active chromatin, in LNCaP-AR cells showed a significant loss of acetylation in response to BG-15n at AR-binding regions but not at regions lacking AR (*SI Appendix*, Fig. S12 *A–C*). Surveying all acetylation changes, AR-binding sites were only present at sites of H3K27ac loss (Fig. 5 *C* and *D*).

Long-range 3D interactions between enhancers and promoters are critical in maintaining oncogene expression in prostate cancer (43). This phenomenon was apparent at the PSA enhancer region where *KLK3* and *KLK2* had AR binding in their promoter and

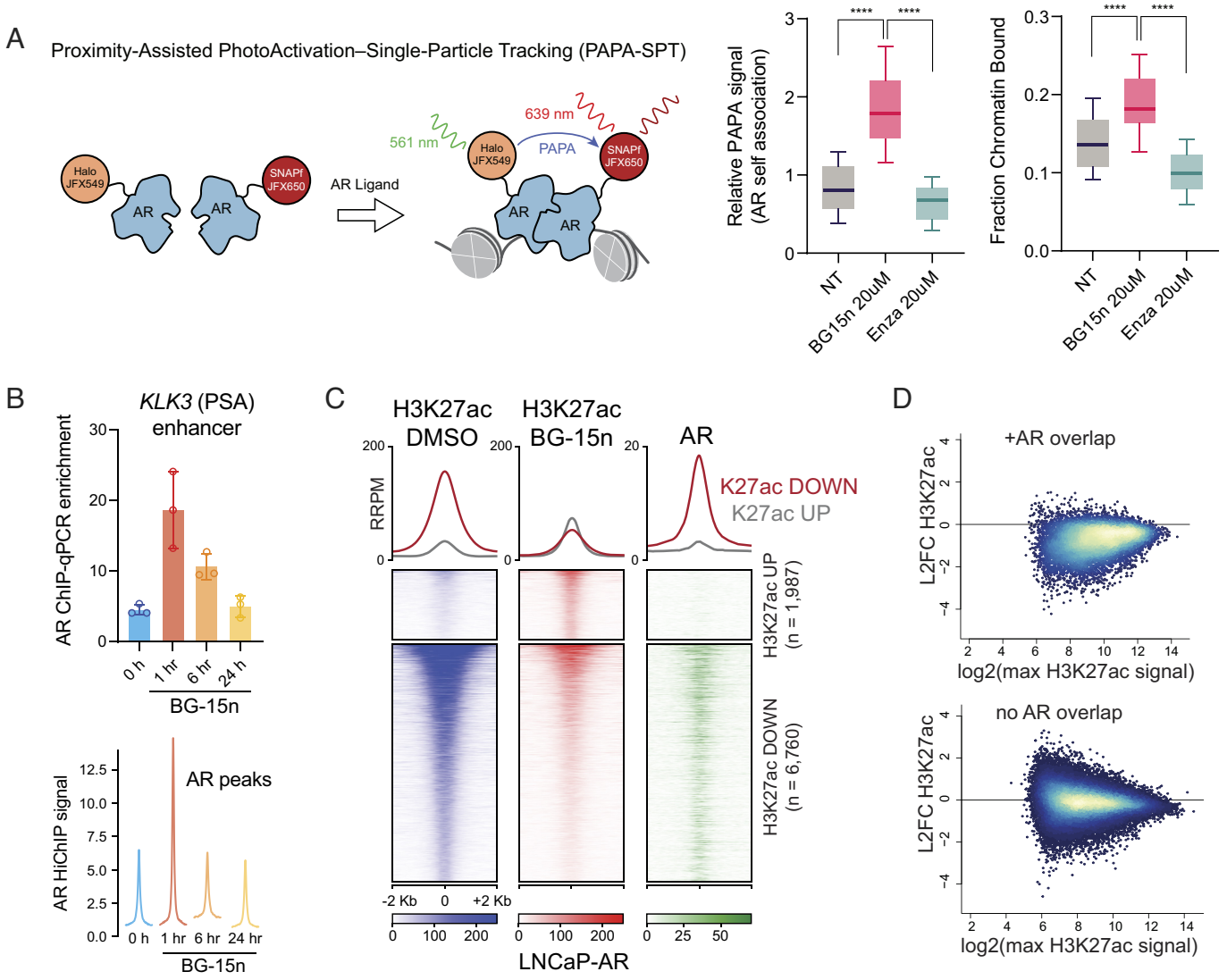

Fig. 5. BG-15n modulates AR chromatin binding and histone acetylation. (*A*) Analysis of AR chromatin binding and self-association using PAPA and fast single-molecule tracking (fSMT). *Left* panel: Working principle of PAPA. Excitation of a sender fluorophore coupled to Halo-AR reactivates an adjacent receiver fluorophore coupled to SNAPf-AR, providing a measure of AR self-association. Relative PAPA signal (*Middle* panel) and overall fraction bound of SNAPf-AR (*Right* panel) in cells coexpressing Halo-AR and SNAPf-AR that were treated with the indicated drugs at 20 μM for 6 h. (*B*) AR ChIP-qPCR (*Top*) and AR HiChIP (*Bottom*) at the PSA enhancer region in LNCaP-AR cells. Cells treated with BG-15n for 1, 6, or 24 h, and compared to matched DMSO. Boxplot shows means and SD of triplicates per condition. (*C*) Heatmap of H3K27ac signal (CUT&RUN) in LNCaP-AR cells with BG-15n treatment (30 μM, 48 h) compared to DMSO, and greater AR binding in regions of H3K27ac loss. (*D*) MA plot comparison for log2(Fold Change, BG15n vs. DMSO) of H3K27ac binding (RRPM) compared to maximum H3K27ac signal with or without AR binding overlap. MA plot; log ratio and mean average scale plot. CUT&RUN data generated from LNCaP-AR cells with BG-15n treatment (30 μM, 48 h) or DMSO.

were part of a large H3K27ac cluster within a CTCF-defined TAD region (Fig. 6*A*). Given the chromatin alterations induced by BG-15n, we performed HiChIP in LNCaP-AR cells to interrogate the 3D-architectural changes mediated by AR and H3K27ac upon BG-15n treatment. We further quantified AR, H3K27ac, and CTCF connectivity between insulators, enhancers, and promoters. CTCF marked topologically associated domain (TAD) boundaries (44) (92% of the regional connectivity); our results clearly showed that only 2 to 4% of interactions were between enhancers and promoters (Fig. 6*B*). CTCF demonstrated a strong 3D connection at the 5′ and 3′ of TAD borders (*SI Appendix*, Fig. S12*D*), H3K27ac showed 49% enhancer–enhancer loop connectivity and 45% enhancer–promoter connectivity (Fig. 6*B*). AR HiChIP experiments were sensitive to salt concentrations, and medium-salt washing maximized short and long-range cluster distribution (*SI Appendix*, Fig. S1). Next, we validated AR HiChIP by comparing enrichment at sites of known AR ChIP-seq binding and found strong coenrichment between AR HiChIP and public AR ChIP-seq datasets (*SI Appendix*, Fig. S12*E*). The AR exhibited 57% enhancer–enhancer looping, 12% enhancer–promoter, 31% promoter–promoter, and no insulator looping (Fig. 6*B*), providing a map for interrogating BG-15n drug influence.

We noticed that many BG-15n responsive genes featured AR bound to H3K27ac sites that were forming expansive networks of connectivity across adjacently looped enhancers and promoters. We therefore grouped regions of extensive overlapping loops into "clusters" and compared them to isolated loops and peaks using our GRACE algorithm (45). Clusters are inclusive of H3K27ac loops for both enhancers and promoters and mark the most active regions of the epigenome (*SI Appendix*, Fig. S13*A*). All drug/control-treated HiChIP experiments were performed with spike-in of mouse chromatin to allow for absolute quantification of architecture (AQuA) (46). BG-15n eliminated many of these clusters (*SI Appendix*, Fig. S13*B*), and genes with the strongest H3K27ac clustering were most down-regulated by BG-15n (*SI Appendix*, Fig. S13*C*). H3K27ac clusters also harbored the

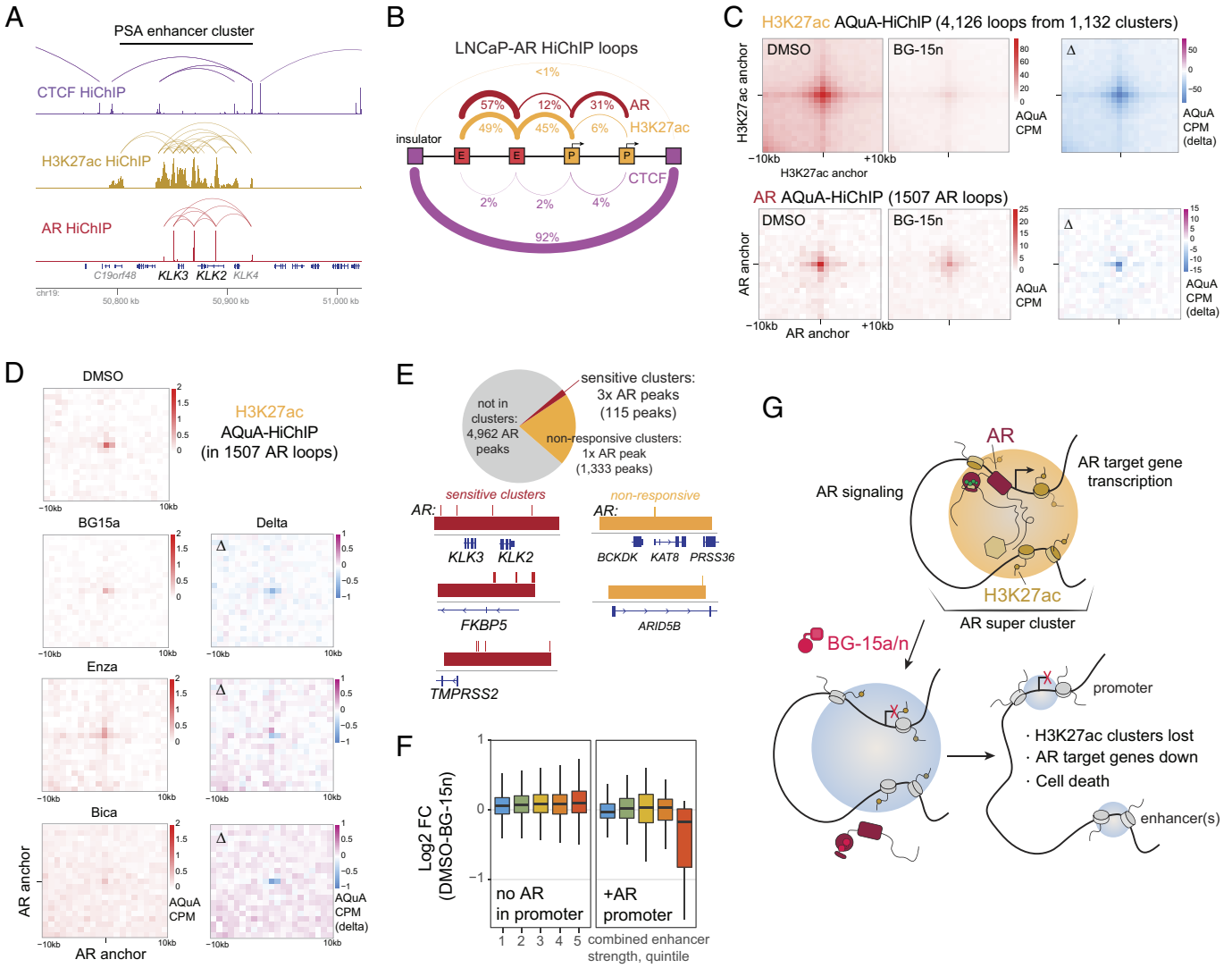

Fig. 6. BG-15n causes the AR to suppress H3K27ac enhancer clusters. (*A*) Genome browser view of the PSA cluster containing KLK2 and KLK3, showing H3K27ac clustered loops and associated HiChIP signal, AR loops and associated AR HiChIP signal, and CTCF loops with associated CTCF HiChIP signal. (*B*) LNCaP-AR HiChIP identified genome-wide loops for AR, H3K27ac, and CTCF binding across promoters, enhancers, or insulators. Represented as percentages of total connectivity. (*C*) APA (Aggregate Peak Analysis) plots for H3K27ac AQuA-HiChIP (*Top*) and AR AQuA-HiChIP (*Bottom*) in LNCaP-AR cells treated with DMSO (*Left*), BG-15n (*Center*), or the delta of BG-15n compared to DMSO (*Right*). BG-15n treatment was for 24 h at 20 μM in LNCaP-AR cells. AQuA CPM is represented as bins of ±1 kB or H3K27ac or AR anchors (*Top*). AQuA, Absolute Quantification of Architecture; CPM, contacts per million. (*D*) Change in H3K27ac AQuA-HiChIP signal at AR loops after treatment with BG-15a, enzalutamide, or bicalutamide. Each treatment was for 24 h at 20 μM in LNCaP-AR cells. (*E*) Pie-chart of gene sensitivity to BG-15n treatment based on inclusion in a peak cluster. Example AR-target genes shown below for responsive genes in clusters with multiple AR peaks, and nonresponsive genes in clusters having only one AR peak. (*F*) Responsiveness of genes to BG-15n grouped by quantile of combined enhancer strength (H3K27ac deposition), either without (*Left*) or with AR binding to each gene's promoter region (*Right*). RNA-seq was performed with DMSO or BG-15n treatment for 24 h at 20 μM in LNCaP-AR cells. (*G*) Model of BG15n action, causing AR to localize to enhancer–promoter regions of prostate cancer genes, but shutting down active H3K27ac and chromatin folding.

greatest amount of overlapping AR peaks (*SI Appendix*, Fig. S13*D*). Aggregate peak analysis (APA) centered on looped pairs within clusters reveal that BG-15n causes a loss of 3D-contact frequency for both H3K27ac and the AR (Fig. 6*C*). H3K27ac HiChIP further revealed BG15a and bicalutamide decreased long-range acetylation contacts at AR loops, as did enzalutamide to a lesser extent (Fig. 6*D*). Some examples of AR-target genes that undergo H3K27ac cluster collapse upon BG15n treatment include *KLK2*/*KLK3*, *FKBP5*, and *LPAR3* (*SI Appendix*, Fig. S13*E*).

Only approximately 200 genes are AR-ligand regulated, yet there are over 6,000 canonical AR-binding sites in the PCa epigenome (47). We wondered whether the explanation for the discrepancy is that AR alone is not sufficient to regulate the gene expression, but that cluster formations are a corequirement. We found that most AR peaks are not in clusters and are also not associated with AR-regulated genes. In addition, 1,333 AR peaks of the 6,000 AR-binding sites were found within AR-ligand nonresponsive clusters only having 1× AR peak per cluster (Fig. 6*E*). In contrast, 115 AR peaks in the 44 most ligand-sensitive clusters have, on average, 3× AR peaks in each cluster (Fig. 6*E*). These clusters include well-known PCa genes such as *KLK3*, *TMPRSS2*, and *FKPB5*. Genes with both AR binding in the promoter and regulatory architecture comprising exceptionally strong enhancers (highest H3K27ac abundance), were most responsive to BG-15n (Fig. 6*F*).

BG-15n treatment resulted in a loss of both AR (*SI Appendix*, Fig. S13*F*) and H3K27ac (*SI Appendix*, Fig. S13*G*) connectivity between adjacent enhancer regions (E to E) and between enhancer and promoter regions (E to P). To understand the mechanism by which AR perturbation was driving the acetylation loss, we investigated AR-binding partner changes in response to BG-15a/n treatment. Using both immunoprecipitation-mass spectrometry (IP-MS) and rapid immunoprecipitation and mass spectrometry

of endogenous protein (RIME) assays, we pulled-down AR from PCa cells following BG-15a/n or agonist treatment. Notably, agonist treatment recruited a high abundance of chromatin activators, as expected, but BG-15n treatment failed to recruit the activators to AR (*SI Appendix*, Fig. S14*A*). The reduced recruitment of coregulator proteins was specific to chromatin machinery, especially BAF complex subunits (*SI Appendix*, Fig. S14*B*). BAF subunits SMARCA4, SMARCE1, and ARID1A were recruited by agonists, but not by BG-15a/n across two models (*SI Appendix*, Fig. S14 *E* and *F*). Indeed, the BAF complex is cobound with AR across the epigenome of prostate cancer, including the *KLK3* enhancer, and BG15a decreased binding of both SMARCA4 and ARID1A at this site (*SI Appendix*, Fig. S15).

Together, our data show that BG-15a/n allows for a temporary recruitment of AR to target genes, but once there, blocks binding of chromatin machinery resulting in a selective repression of expression of genes with AR in their promoters by loss of chromatin contacts to active enhancers within the transcriptional cluster (Fig. 6*G*).

Discussion

The unmet clinical challenge of managing treatment-resistant mCRPC that still rely on AR signaling mandates the development of novel AR-targeted therapies, such as AR-NTD inhibitors (48), or PROteolysis TArgeting Chimeras (PROTACs) (49) and others. The AR antagonists we developed have mechanistic features that expand the repertoire of available AR targeting agents. BG15a/n molecules bind the AR, induce changes to chromatin activity, and halt AR-transcriptional output. They are unique in their ability to induce AR dimerization, AR-nuclear translocation across multiple experimental assays, and increased AR-chromatin binding. The BG-series molecules share the same cyanonilutamide scaffold as enzalutamide and apalutamide. The molecular feature that appears responsible for AR-nuclear localization is the flexibility in the molecule that other antagonists lack which we confirmed by making a nonflexible derivative that lost this ability (Fig. 2*B*). BG-15a/n share the ability of other ARSIs to disrupt AR-target gene expression and have a greater impact on MYC-target genes than current ARSIs.

BG-15a and BG-15n have AR binding superior to clinical ARSI enzalutamide, strongly and selectively inhibit AR-dependent transcription, and yet also induce rapid translocation of AR to the nucleus, AR self-association, and chromatin binding (unlike traditional antagonists that work by impairing AR-nuclear translocation and hindering AR self-association and/or chromatin binding). Mechanistically, the collapse of active 3D *cis*-regulatory clusters is a key feature of BG-15a/s mechanisms of action. Recent work employing 3D-genomic approaches to the role of AR in prostate cancer posits that ligand-driven induction of AR into the nucleus tends to strengthen existing contacts rather than create novel ones (50). This is consistent with similar work carried out on glucocorticoid receptor (51) and estrogen receptor (52). In contrast with these effects of nuclear hormone receptor agonists, AR loops and the associated H3K27ac loops are lost after treatment with BG15n.

Importantly, we have defined the genomic features required for transcriptional response to AR ligands: the presence of a strong 3D-enhancer cluster along with multiple AR-binding sites across both enhancers and promoters. These data, coupled with further validation, will be critical for understanding long-range transcriptional requirements of CRPC development and drug resistance.

Our findings highlight the unique mechanism of action of BG15a and BG-15n in modulating AR-transcriptional activity and chromatin architecture. However, we acknowledge that the observed effects on cell proliferation in vitro and tumor progression in vivo may be partially influenced by off-target activities of these compounds. While we have demonstrated the selectivity of BG-15a/n for AR using radioligand binding assays and assessed its impact on other nuclear hormone receptors, the possibility of off-target interactions cannot be entirely ruled out. Future studies will aim to further elucidate the specificity and selectivity of these compounds.

In summary, the majority of advanced mCRPC tumors still depend on AR signaling and represent a disease context in need of further therapeutics strategies. The novel compounds, such as BG-15n, can strongly down-regulate expression of AR-target genes, convert AR, the main driver of tumor progression into a therapeutic ally, and warrant further investigation for their translational promise.

Methods

AR Binding Assays. Radioligand binding (Eurofins Panlabs) was performed using steroid hormone receptors and respective ligands in buffer (50 mM Tris-HCl, 0.8 M NaCl, 10% glycerol, 2 mM dithiothreitol, 0.1% BSA, and 2% EtOH, pH 7.4). First, receptors were incubated with ligands, then incubated with a hydroxyapatite slurry over 15 min, and filtered. The filters were then washed 3 times and counted to determine ligand specifically bound. Compounds were tested in a logarithmic concentration range from 10 nM to 100 μM to determine K_i and IC_{50} values.

Cell Culture. The human embryonic kidney cell line HEK 293T was purchased from ATCC and cultured in DMEM with 10% fetal bovine serum (FBS). LNCaP and 22Rv1 cells (ATCC) were maintained in RPMI-1640 (Gibco, 11875119) supplemented with 10% fetal bovine serum (FBS) (Gibco, A3160402). LAMP cells (clone 122, a kind gift from David Takeda) and LNCaP-AR cells (a kind gift from Charles Sawyers) were maintained in DMEM with 10% FBS, 1X penicillin–streptomycin–glutamine (Thermo Fisher, 10378016). PC3 cells were maintained in Ham's F-12 K media (Gibco, 21127022) supplemented with 10% fetal bovine serum. All cells tested negative for *Mycoplasma* (Universal *Mycoplasma* Detection Kit, ATCC, 30-1012K) and were maintained in a 37 °C incubator with 5% CO_2. All cell line identities were confirmed by STR.

Transfection and Luciferase Assay for AR Activity. The reporter plasmid, pARLuc, was purchased from Signosis and contains firefly luciferase downstream of AR response elements. VCaP or LNCaP cells were cultured in DMEM (ATCC) with 5% FBS (Gibco) or 5% CSS (Gibco) to an approximate confluence of 70% in 96-well plates. Cells were then transiently transfected with 100 ng of pARLuc plasmid per well using Lipofectamine 3000 transfection reagent (Invitrogen). Following 24 h of incubation at 37 °C, the cells were dosed with a range of 0 to 20 μM (order of magnitude) BG-15a, BG-15n, or enzalutamide. For antagonism assays, 10 nM R1881 was added to all wells in addition to antagonist ligand at previously described concentrations. After 24 h of incubation at 37 °C, cells were lysed using Promega Bright-Glo Reagent (1:1) and luminescence was measured using a Thermo Scientific Varioskan LUX plate reader. Data reported represent the average of triplicates.

PAPA with Fast Single-Molecule Tracking. The PAPA with fast single-molecule tracking (PAPA-fSMT) assays were performed using the automated imaging system and cell culture conditions described in detail elsewhere (53). In brief, a transgenic U2OS cell line coexpressing Halo- and SNAPf-tagged mouse AR (41) was labeled overnight with a mixture of 50 nM Janelia Fluor X 549 (JFX549) Halo ligand and 5 nM Janelia Fluor X 650 SNAP ligand in phenol red-free DMEM. The indicated drugs were added 6 h before imaging. Cells were destained twice for 30 min and subjected to a final medium change, all in the presence of the drug. A 5-cycle PAPA-fSMT protocol (53) was employed using 7 ms pulses for 561 nm and 405 nm reactivation. Single molecules were localized and tracked using quot (https://github.com/alecheckert/quot). The PAPA signal was quantified as the ratio of the number of fluorophores reactivated by 561 nm excitation (PAPA) to the number reactivated by proximity-independent direct reactivation with 405 nm light. This signal was then normalized to a nontreated control. The fraction chromatin bound in each cell was determined by performing state array analysis

on direct-reactivated trajectories from each cell (https://github.com/alecheckert/saspt) (54) and summing the total state array occupancy below a diffusion coefficient of 0.1 $\mu m^2/s$.

Analysis of 3D Loops and Clusters. HiChIP was performed with the Dovetail MNase-HiChIP kit, and each sample was paired-end sequenced to a minimum depth of 200 million reads. For analysis of 3D loops, the Peaks3D pipeline (https://github.com/GryderLab/peaks3d) was used to read HiChIP .hic files to make 3D clusters. Filtered loops were made based on the predefined thresholds such as min/max distance restrictions, minimum AQuA-CPM, and the minimum number of connections per cluster. Filtered loops were then merged into a cluster where a path between any ends of the loops was drawn. Briefly, the clustering program began at any loop in the filtered loop set, recursively searched all the loops connected to the left or right ends, and assigned the same cluster ID to the visited ends. This was completed for all unvisited loops with a unique cluster ID. The result was 2D peaks, loops (<min_loops), and clusters (≥ min_loops), within a given user-defined threshold, min_loops. After clustering, these three elements were ranked by the 3D connectivity estimated by the sum of short and long 3D contacts within the expanded boundary (e.g., min and max coordinates of the cluster). This procedure was run iteratively and the pipeline produced intermediate files such as filtered bedpe, clustered density, QC visualization, and APA plots for user validation.

For additional information for experiments, including detailed synthetic routes and compound characterization, immunofluorescence, molecular docking, ChIP-qPCR, ChIP-seq RNA-seq, CUT&RUN, HiChIP, AQuA-HiChIP, in vitro cell growth experiments, ex vivo and in vivo models, and pharmacokinetic experiments, please see *SI Appendix, Materials and Methods*.

Data, Materials, and Software Availability. All raw next-generation sequencing, ChIP-seq, CUT&RUN, RNA-seq, and HiChIP data generated in this study have been deposited in the Gene Expression Omnibus (GEO) repository at NCBI under Accession Code GSE205980 (55). Custom software developed to analyze CUT&RUN, ChIP-seq, RNA-seq, to call loops and clusters from peaks in HiChIP and AQuA-HiChIP data, and to visualize these data is available in our GitHub repository https://github.com/GryderLab/ (56).

ACKNOWLEDGMENTS. We would like to thank the Case Western Reserve University Genomics Core, especially Simone Edelheit, for the assistance in RNA sequencing, cleavage under targets and release using nuclease (CUT&RUN) sequencing, and ChIP-qPCR, Pete Schacheri's lab for reagents and guidance in CUT&RUN, University at Buffalo Genomics and Bioinformatics Core for RNA-sequencing of treated LuCaP models, and David Takeda for the Lamp122 cell line. We also acknowledge Brian Biggs for assistance with synthesis. We also thank Jorma Palvimo and Kaisa-Mari Launonen at the University of Eastern Finland School of Medicine for their assistance with the rapid immunoprecipitation mass spectrometry of endogenous protein (RIME) experiments and Eva Estébanez-Perpiñá and Alba Jiménez-Panizo from the Institute of Biomedicine of the University of Barcelona for providing purified Androgen Receptor protein. We thank the Case Western Reserve University School of Medicine Light Microscopy Core Facility which is supported by the NIH Grant S10-OD024996 for the assistance in confocal microscopy images. This work was supported by the following mechanisms: P.S.N. is supported by CA097186, CA163227, PC230420, and the Prostate Cancer Foundation; A.K.O. is supported by the Vasser-Woolley Faculty Fellowship, 5R01CA266013-03, and Georgia Tech; R.A.-O. is supported by W81XWH-19-1-0715, Kaleida Health Foundation, and Prostate Cancer Foundation; B.E.G. is supported by 1K22CA255594, and 5R01CA291963-02; and E.C. is supported by P50CA97186, CA163227 and Institute of Prostate cancer Research.

Author affiliations: [a]Cancer Genomics and Epigenomics Program, Case Comprehensive Cancer Center, Case Western Reserve University, Cleveland, OH 44106; [b]Department of Pharmacology, Case Western Reserve University School of Medicine, Cleveland, OH 44106; [c]Parker H. Petit Institute for Bioengineering and Biosciences, Department of Chemistry and Biochemistry, Georgia Institute of Technology, Atlanta, GA 30332; [d]Clinical Pharmacology Program, Center for Cancer Research, National Cancer Institute, NIH, Bethesda, MD 20892; [e]Department of Nutrition, Case Western Reserve University School of Medicine, Cleveland, OH 44106; [f]Department of Genetics and Genome Sciences, Case Western Reserve University School of Medicine, Cleveland, OH 44106; [g]Alphazyme, Jupiter, FL 33458; [h]Laboratory of Receptor Biology and Gene Expression, Center for Cancer Research, National Cancer Institute, NIH, Bethesda, MD 20892; [i]Department of Urology, University of Washington, Seattle, WA 98195; [j]Department of Cellular and Physiological Sciences, Life Sciences Institute, University of British Columbia, Vancouver, BC V6T 1Z3, Canada; [k]Department of Genetics, Perelman School of Medicine, University of Pennsylvania, Philadelphia, PA 19104; [l]Axiotl Inc., Cleveland, OH 44106; [m]Department of Medicine, University of Washington, Seattle, WA 98195; [n]Division of Human Biology and Clinical Research, Fred Hutchinson Cancer Center, Seattle, WA 98109; [o]Division of Clinical Research, Fred Hutchinson Cancer Center, Seattle, WA 98109; [p]Laboratory for Genitourinary Cancer Pathogenesis, Center for Cancer Research, National Cancer Institute, NIH, Bethesda, MD 20892; [q]Department of Molecular and Cell Biology, University of California, Berkeley, CA 94720; and [r]Division of Hematology and Oncology, Department of Medicine, Jacobs School of Medicine and Biomedical Sciences, University at Buffalo, State University of New York, Buffalo, NY 14203

Author contributions: S.E.K., B.W., A.K., R.S., T.G.W.G., W.D.F., A.K.O., E.C., R.A.-O., and B.E.G. designed research; S.E.K., E.J.N., S.T., B.W., J.S., M.S.C., D.G., M. Rood, E.R., D.S., H.M.N., L.G.B., M. Ramser, C.P., W.M.M., N.A., T.G.W.G., E.C., R.A.-O., and B.E.G. performed research; S.T., B.W., E.R., P.S.N., K.K.K., X.D., A.K.O., and B.E.G. contributed new reagents/analytic tools; S.E.K., E.J.N., B.W., J.S., Y.A., H.K., M.S.C., M.C., R.S., T.G.W.G., R.A.-O., and B.E.G. analyzed data; and S.E.K., B.W., E.C., R.A.-O., and B.E.G. wrote the paper.

1. R. Siegel, D. Naishadham, A. Jemal, Cancer statistics, 2012. *CA Cancer J. Clin.* **62**, 10–29 (2012), 10.3322/caac.20138.
2. G. Pirtskhalaishvili, R. L. Hrebinko, J. B. Nelson, The treatment of prostate cancer–An overview of current options. *Cancer Pract.* **9**, 295–306 (2001).
3. E. S. Antonarakis *et al.*, AR-V7 and resistance to enzalutamide and abiraterone in prostate cancer. *N. Engl. J. Med.* **371**, 1028–1038 (2014), 10.1056/NEJMoa1315815.
4. L. Merkens *et al.*, Aggressive variants of prostate cancer: Underlying mechanisms of neuroendocrine transdifferentiation. *J. Exp. Clin. Cancer Res.* **41**, 46 (2022), 10.1186/s13046-022-02255-y.
5. C. D. Chen *et al.*, Molecular determinants of resistance to antiandrogen therapy. *Nat. Med.* **10**, 33–39 (2004), 10.1038/nm972.
6. A. G. Papatsoris, M. V. Karamouzis, A. G. Papavassiliou, Novel biological agents for the treatment of hormone-refractory prostate cancer (HRPC). *Curr. Med. Chem.* **12**, 277–296 (2005).
7. M. J. Linja *et al.*, Amplification and overexpression of androgen receptor gene in hormone-refractory prostate cancer. *Cancer Res.* **61**, 3550–3555 (2001).
8. D. Y. Takeda *et al.*, A somatically acquired enhancer of the androgen receptor is a noncoding driver in advanced prostate cancer. *Cell* **174**, 422–432.e413 (2018).
9. N. J. McKenna, B. W. O'Malley, Combinatorial control of gene expression by nuclear receptors and coregulators. *Cell* **108**, 465–474 (2002).
10. B. Gryder, P. C. Scacheri, T. Ried, J. Khan, Chromatin mechanisms driving cancer. *Cold Spring Harb. Perspect. Biol.* **14**, a040956 (2021), 10.1101/cshperspect.a040956.
11. E. V. Wasmuth *et al.*, Allosteric interactions prime androgen receptor dimerization and activation. *Mol. Cell* **82**, 2021–2031.e5 (2022).
12. S. Stelloo, A. M. Bergman, W. Zwart, Androgen receptor enhancer usage and the chromatin regulatory landscape in human prostate cancers. *Endocr. Relat. Cancer* **26**, R267–R285 (2019), 10.1530/ERC-19-0032.
13. K.-M. Launonen *et al.*, Chromatin-directed proteomics-identified network of endogenous androgen receptor in prostate cancer cells. *Oncogene* **40**, 4567–4579 (2021), 10.1038/s41388-021-01887-2.
14. J. D. Debes, L. J. Schmidt, H. Huang, D. J. Tindall, p300 mediates androgen-independent transactivation of the androgen receptor by interleukin 6. *Cancer Res.* **62**, 5632–5636 (2002).
15. P. C. Echeverria, D. Picard, Molecular chaperones, essential partners of steroid hormone receptors for activity and mobility. *Biochim. Biophys. Acta Mol. Cell Res.* **1803**, 641–649 (2010), 10.1016/j.bbamcr.2009.11.012.
16. S. C. Biddie, S. John, G. L. Hager, Genome-wide mechanisms of nuclear receptor action. *Trends Endocrinol. Metab.* **21**, 3–9 (2010).
17. C. M. Armstrong, A. C. Gao, Current strategies for targeting the activity of androgen receptor variants. *Asian J. Urol.* **6**, 42–49 (2019), 10.1016/j.ajur.2018.07.003.
18. S. Prekovic *et al.*, Molecular underpinnings of enzalutamide resistance. *Endocr. Relat. Cancer* **25**, R545 (2018), 10.1530/erc-17-0136.
19. A. Vander Ark, J. Cao, X. Li, Mechanisms and approaches for overcoming enzalutamide resistance in prostate cancer. *Front. Oncol.* **8**, 180–180 (2018), 10.3389/fonc.2018.00180.
20. C. Tran *et al.*, Development of a second-generation antiandrogen for treatment of advanced prostate cancer. *Science* **324**, 787–790 (2009), 10.1126/science.1168175.
21. N. J. Clegg *et al.*, ARN-509: A novel antiandrogen for prostate cancer treatment. *Cancer Res.* **72**, 1494–1503 (2012), 10.1158/0008-5472.can-11-3948.
22. M. R. Smith *et al.*, Darolutamide and survival in metastatic, hormone-sensitive prostate cancer. *N. Engl. J. Med.* **386**, 1132–1142 (2022), 10.1056/NEJMoa2119115.
23. M. D. Balbas *et al.*, Overcoming mutation-based resistance to antiandrogens with rational drug design. *eLife* **2**, e00499 (2013), 10.7554/eLife.00499.
24. T. Hara *et al.*, Novel mutations of androgen receptor: A possible mechanism of bicalutamide withdrawal syndrome. *Cancer Res.* **63**, 149–153 (2003).
25. J. D. Joseph *et al.*, A clinically relevant androgen receptor mutation confers resistance to second-generation antiandrogens enzalutamide and ARN-509. *Cancer Discov.* **3**, 1020–1029 (2013).
26. E. C. Dreaden *et al.*, Antiandrogen gold nanoparticles dual-target and overcome treatment resistance in hormone-insensitive prostate cancer cells. *Bioconjug. Chem.* **23**, 1507–1512 (2012), 10.1021/bc300158k.
27. B. E. Gryder *et al.*, Selectively targeting prostate cancer with antiandrogen equipped histone deacetylase inhibitors. *ACS Chem. Biol.* **8**, 2550–2560 (2013), 10.1021/cb400542w.
28. N. J. Clegg *et al.*, ARN-509: A novel antiandrogen for prostate cancer treatment. *Cancer Res.* **72**, 1494–1503 (2012), 10.1158/0008-5472.Can-11-3948.

29. W. Gao, C. E. Bohl, J. T. Dalton, Chemistry and structural biology of androgen receptor. *Chem. Rev.* **105**, 3352–3370 (2005), 10.1021/cr020456u.
30. J. Zhou, B. Liu, G. Geng, J. H. Wu, Study of the impact of the T877A mutation on ligand-induced helix-12 positioning of the androgen receptor resulted in design and synthesis of novel antiandrogens. *Proteins* **78**, 623–637 (2010), 10.1002/prot.22592.
31. M. Nadal *et al.*, Structure of the homodimeric androgen receptor ligand-binding domain. *Nat. Commun.* **8**, 14388 (2017), 10.1038/ncomms14388.
32. Z. Lin *et al.*, Evolutionary-scale prediction of atomic-level protein structure with a language model. *Science* **379**, 1123–1130 (2023), 10.1126/science.ade2574.
33. O. Trott, A. J. Olson, AutoDock Vina: Improving the speed and accuracy of docking with a new scoring function, efficient optimization, and multithreading. *J. Comput. Chem.* **31**, 455–461 (2010), 10.1002/jcc.21334.
34. H. I. Scher *et al.*, Antitumour activity of MDV3100 in castration-resistant prostate cancer: A phase 1–2 study. *Lancet* **375**, 1437–1446 (2010), 10.1016/s0140-6736(10)60172-9.
35. H. I. Scher *et al.*, Increased survival with enzalutamide in prostate cancer after chemotherapy. *N. Engl. J. Med.* **367**, 1187–1197 (2012), 10.1056/NEJMoa1207506.
36. T. I. Klokk *et al.*, Ligand-specific dynamics of the androgen receptor at its response element in living cells. *Mol. Cell. Biol.* **27**, 1823–1843 (2007), 10.1128/MCB.01297-06.
37. D. W. Baggett *et al.*, An image analysis pipeline for quantifying the features of fluorescently-labeled biomolecular condensates in cells. *Front. Bioinf.* **2**, 897238 (2022), 10.3389/fbinf.2022.897238.
38. M. Korpal *et al.*, An F876L mutation in androgen receptor confers genetic and phenotypic resistance to MDV3100 (Enzalutamide). *Cancer Discov.* **3**, 1030–1043 (2013), 10.1158/2159-8290.CD-13-0142.
39. J. A. Pollock *et al.*, Inhibiting androgen receptor nuclear entry in castration-resistant prostate cancer. *Nat. Chem. Biol.* **12**, 795–801 (2016), 10.1038/nchembio.2131.
40. J. A. Gibbons *et al.*, Clinical pharmacokinetic studies of enzalutamide. *Clin. Pharmacokinet.* **54**, 1043–1055 (2015), 10.1007/s40262-015-0271-5.
41. T. G. W. Graham, J. J. Ferrie, G. M. Dailey, R. Tjian, X. Darzacq, Detecting molecular interactions in live-cell single-molecule imaging with proximity-assisted photoactivation (PAPA). *eLife* **11**, e76870 (2022), 10.7554/eLife.76870.
42. S. Henikoff, J. G. Henikoff, H. S. Kaya-Okur, K. Ahmad, Efficient chromatin accessibility mapping in situ by nucleosome-tethered tagmentation. *eLife* **9**, e63274 (2020), 10.7554/eLife.63274.
43. L. Xiao *et al.*, Targeting SWI/SNF ATPases in enhancer-addicted prostate cancer. *Nature* **601**, 434–439 (2022), 10.1038/s41586-021-04246-z.
44. S. S. P. Rao *et al.*, A 3D map of the human genome at kilobase resolution reveals principles of chromatin looping. *Cell* **159**, 1665–1680 (2014).
45. Y. Asante *et al.*, PAX3-FOXO1 uses its activation domain to recruit CBP/P300 and shape RNA Pol2 cluster distribution. *Nat. Commun.* **14**, 8361 (2023), 10.1038/s41467-023-43780-4.
46. B. E. Gryder, J. Khan, B. Z. Stanton, Measurement of differential chromatin interactions with absolute quantification of architecture (AQuA-HiChIP). *Nat. Protoc.* **15**, 1209–1236 (2020), 10.1038/s41596-019-0285-9.
47. H. J. Jin, J. Kim, J. Yu, Androgen receptor genomic regulation. *Transl. Androl. Urol.* **2**, 157–177 (2013), 10.3978/j.issn.2223-4683.2013.09.01.
48. N. H. Hong *et al.*, The preclinical characterization of the N-terminal domain androgen receptor inhibitor, EPI-7386, for the treatment of prostate cancer. *Eur. J. Cancer* **138**, S51 (2020), 10.1016/S0959-8049(20)31212-0.
49. T. Neklesa *et al.*, Abstract 5236: ARV-110: An androgen receptor PROTAC degrader for prostate cancer. *Cancer Res.* **78**, 5236–5236 (2018), 10.1158/1538-7445.Am2018-5236.
50. N. Lack *et al.*, Decoding the epigenetics and chromatin loop dynamics of androgen receptor-mediated transcription. bioRxiv [Preprint] (2024). https://doi.org/10.1101/2023.12.22.573134. Accessed 5 July 2024.
51. A. M. D'Ippolito *et al.*, Pre-established chromatin interactions mediate the genomic response to glucocorticoids. *Cell Syst.* **7**, 146–160.e147 (2018), 10.1016/j.cels.2018.06.007.
52. S. Kocanova *et al.*, Enhancer-driven 3D chromatin domain folding modulates transcription in human mammary tumor cells. *Life Sci. Alliance* **7**, e202302154 (2024), 10.26508/lsa.202302154.
53. T. G. W. Graham *et al.*, Single-molecule live imaging of subunit interactions and exchange within cellular regulatory complexes. bioRxiv [Preprint] (2024), https://doi.org/10.1101/2024.06.25.600644. Accessed 1 July 2024.
54. A. Heckert, L. Dahal, R. Tjian, X. Darzacq, Recovering mixtures of fast-diffusing states from short single-particle trajectories. *eLife* **11**, e70169 (2022), 10.7554/eLife.70169.
55. B. E. Gryder, H. Kim, Inverse agonists of the androgen receptor. GEO. https://www.ncbi.nlm.nih.gov/geo/query/acc.cgi?acc=GSE205980. Deposited 13 June 2022.
56. B. E. Gryder, Gryder Lab Software. Github Code Repository. https://github.com/GryderLab/. Accessed 3 October 2024.